PNAS RESEARCH ARTICLE | BIOPHYSICS AND COMPUTATIONAL BIOLOGY

Lipoprotein diffusion in dense yolk plasma is governed by softness, hydrodynamics, and caging: Insights from MHz-XPCS

Nimmi Das Anthuparambil[a,b,1], Michelle Dargasz[a], Sonja Timmermann[a], Anita Girelli[c], Sebastian Retzbach[d], Johannes Möller[e], Wonhyuk Jo[e], Agha Mohammad Raza[a], Aliaksandr Leonau[a,e], James Wrigley[e], Frederik Unger[a,b], Maddalena Bin[c], Prince Prabhu Rajaiah[f,g], Iason Andronis[c], William Chèvremont[h], Jörg Hallmann[e], Angel Rodriguez-Fernandez[e], Jan-Etienne Pudell[e], Felix Brausse[e], Ulrike Boesenberg[e], Mohamed Youssef[e], Roman Shayduk[e], Rustam Rysov[e], Anders Madsen[e], Felix Lehmkühler[b], Michael Paulus[i], Fajun Zhang[d], Fivos Perakis[c], Frank Schreiber[d], and Christian Gutt[a,1]

Affiliations are included on p. 8.

Edited by Magdaleno Medina-Noyola, Universidad Autonoma de San Luis Potosi, San Luis Potosí, Mexico; received July 23, 2025; accepted January 25, 2026 by Editorial Board Member Paul Chaikin

Low-density lipoproteins (LDLs) are central to nutrient transport in egg yolk and have emerged as natural nanocarriers for drug delivery. Their biological function critically depends on mobility within densely crowded environments, yet the mechanisms governing their motion remain elusive, largely because conventional techniques cannot access the relevant microsecond timescales. Here, we employ megahertz X-ray photon correlation spectroscopy at the European X-ray Free Electron Laser facility to resolve LDL dynamics in native yolk-plasma. This approach reveals transient caging and memory effects and shows that the combined influence of particle softness and hydrodynamic coupling slows diffusion by nearly two orders of magnitude compared to dilute solutions. However, this reduction could not be scaled with an increase in macroscopic viscosity obtained from rheometry, indicating deviations from the Stokes–Einstein relation. Despite this slowdown, yolk-plasma remains a "sluggish yet liquid state", balancing dense packing and the fluidity required for lipid release during embryonic development. These results establish a quantitative framework connecting microstructure, hydrodynamics, and transport in crowded soft-matter systems, with implications for developmental biology and nanomedicine.

macromolecular crowding | anomalous diffusion | megahertz X-ray photon correlation spectroscopy | hydrodynamic interactions | low-density lipoprotein

Significance

Egg yolk is an extremely crowded fluid that stores lipids for the developing embryo, yet the low-density lipoproteins (LDLs) that carry these lipids must still move. Using megahertz X-ray photon correlation spectroscopy, we directly track native LDL motion in yolk-plasma on 0.22 to 69 μs timescales. We find that LDLs become transiently caged, develop memory effects, and diffuse up to 100-fold more slowly than in dilute solution, yet yolk-plasma remains a "sluggish liquid" rather than a solid. We also provide a quantitative description that links LDL softness, crowding, and hydrodynamic coupling to longtime mobility. This framework can be used to assess transport and arrest in other densely packed protein systems, from condensates to therapeutic formulations.

Low-density lipoproteins (LDLs) are core-shell nanoparticles that are central to fat transport in humans and animals, as well as to nutrient delivery in egg yolk (1–3). Egg yolk plasma is a crowded medium with LDL volume fractions exceeding 40%, making particle mobility and viscoelasticity crucial for yolk stability and embryonic development. In human health, hindered LDL diffusion or increased blood viscosity contributes significantly to the formation of atherosclerotic plaques in arterial walls (4, 5). Furthermore, LDLs have attracted substantial attention as promising drug carriers, exhibiting notable advantages over synthetic delivery systems in navigating complex biological media, which is critical for therapeutic efficiency (6–9). Although LDL diffusion is critical in both physiological and pathological contexts, the factors that regulate its behavior in crowded environments remain unclear.

Macromolecular diffusion in densely crowded media, including the cytoplasm, extracellular matrix, and food emulsions, is strongly shaped by intermolecular interactions (10–15). These interactions reduce mobility, generate transient cages, and alter both transport properties and biological function (16–19). Crowding typically increases the effective viscosity through electrostatic, depletion, and hydrodynamic interactions (20–22). At high concentrations, the dynamics become heterogeneous (23, 24) and deviations from the Stokes–Einstein relation indicate a partial decoupling of mass and momentum transport (25, 26). Long- and short-range hydrodynamic interactions (27–31) further introduce correlated motion that acts across multiple timescales (32), though their many-body, flow-mediated nature makes them difficult to model (33).

Crowded protein solutions, phase-separated condensates, and yolk-plasma all share this phenomenology of hindered transport. They are often described in terms of steric crowding, weak attractions, and particle softness, with colloid-based frameworks providing partial insights into their diffusional slowdown (29, 30, 34–39). However, such models remain incomplete for macromolecular assemblies with internal structure,

The authors declare no competing interest.

This article is a PNAS Direct Submission. M.M.-N. is a guest editor invited by the Editorial Board.

[1]To whom correspondence may be addressed. Email: nimmi.das.anthuparambil@desy.de or christian.gutt@uni-siegen.de.

This article contains supporting information online at https://www.pnas.org/lookup/suppl/doi:10.1073/pnas.2519681123/-/DCSupplemental.

Published February 20, 2026.

deformability, and complex surface chemistry (17, 28, 40–42). What is still missing is a quantitative framework that connects the microscopic ingredients of these media—high effective volume fraction, particle softness, and long-range hydrodynamic interactions—to the mesoscopic signatures of caging, memory effects, and collective relaxation on the microsecond timescales and also to the macroscopic transport coefficients that determine how fast such systems reorganize.

Existing experimental techniques typically access either only the very-short time regime, dominated by hydrodynamics, or much longer times, when structural relaxation is complete. The crucial intermediate microsecond window—where particles rattle within local cages and memory effects emerge—has remained unresolved in biological soft matter and crowded protein fluids.

Here, we directly access this missing regime in native egg yolk-plasma and determine how particle softness, crowding, and hydrodynamic interactions jointly regulate LDL transport. Using megahertz X-ray photon correlation spectroscopy (MHz-XPCS) at the European X-ray Free Electron Laser facility (EuXFEL) (43), we probe LDL dynamics in the time scale of 0.22 to 69 μs on molecular length scales. The resulting intermediate scattering functions reveal stretched-exponential relaxation consistent with memory effects arising from both direct interactions and long-range hydrodynamic coupling. We extract a reduced memory function $\Delta(q)$ that strengthens with concentration and exhibits a structured minimum near the principal peak of the static structure factor ($q \approx q_m$), alongside a pronounced minimum in the collective diffusion coefficient $D(q)$ at the same q_m (de Gennes narrowing). This demonstrates that caging and memory are not merely single-particle trapping effects but collective phenomena selected by the cage-scale structure of the suspension.

We further introduce an effective hydrodynamic function $H^*(q)$, which captures the q-dependence of the collective relaxation rates and shows that hydrodynamic interactions remain relevant well beyond the nominal short-time limit, shaping collective relaxation on microsecond time scales. Finally, we connect these mesoscopic observables to macroscopic transport, revealing that LDL self-diffusion in yolk-plasma is suppressed by nearly two orders of magnitude relative to dilute solution, yet the system remains a dense, "sluggish liquid" rather than a glass. This behavior is quantitatively captured by a soft-sphere model (37) with an effective softness parameter and an increased apparent arrest volume fraction. Together, these findings establish a comprehensive framework linking microstructure, memory effects, and long-time diffusion in crowded soft matter systems.

Results

To investigate LDL diffusion under crowded conditions, we use yolk-LDLs in their native suspension form of yolk-plasma, which was extracted from egg yolk via centrifugation (see *Materials and Methods* for details). Fig. 1*A* (*Left* side) illustrates the two distinct fractions obtained after centrifugation: the translucent yolk-plasma fraction floating atop the opaque yolk-granule fraction. The yolk-plasma dry matter comprises approximately ≈85 wt% yolk-LDL particles and ≈15 wt% livetin proteins (44). The LDL particles exhibit a core-shell structure (Fig. 1*A*) with an average radius of ≈15.5 nm (*SI Appendix*, Fig. S3*A*). The original LDL concentration in yolk-plasma was ≈421 mg/ml and was further diluted to two lower concentrations of 378 mg/ml and 336 mg/ml (*Materials and Methods*). Details of the samples are provided in Table 1 and *SI Appendix*, Table S1.

The characteristic interaction time scale is given by the duration required for a particle, with diffusion constant D_0^d, to traverse a distance R comparable to its own size, expressed as $\tau_i = R^2/6D_0^d$. For LDL particles in egg yolk-plasma, this time is approximately $\tau_i \approx 2.5$ μs, assuming $R = 15.5$ nm and $D_0^d = 15.8$ nm^2/μs.

To probe LDL dynamics on this biologically relevant time scale, MHz-XPCS experiments were performed at the Materials Imaging and Dynamics (MID) instrument at the European XFEL, using MHz pulse patterns to probe LDL suspensions. The unique MHz pulse structure of EuXFEL enabled access to a temporal window 0.22 to 69 μs, which encompasses the estimated interaction time scale of 2.5 μs. In addition to XPCS measurements, small-angle X-ray scattering (SAXS) measurements were performed at the ID02 beamline at the European Synchrotron Radiation Facility (ESRF), France. Further details on the MHz-XPCS experiment are provided in *Materials and Methods* and *SI Appendix*. The XPCS measurements provided insights into both structural and dynamical characteristics (45–49) of LDL suspensions, which we present starting with the structural analysis, followed by dynamic properties.

Structural Information. The normalized scattering intensity, $I(q)$, for four concentrations of egg yolk-plasma is shown in Fig. 1*B*. A pronounced peak at $q \approx 0.23$ nm^{-1} is observed in the native yolk-plasma ($c = 421$ mg/ml), reflecting strong interparticle correlations due to the high concentration of LDLs, which account for ≈85 wt% of the plasma's dry matter. The scattering profile of the most diluted sample ($c = 4$ mg/ml) is modeled using a spherical core-shell particle with a core radius of 12 nm and a shell thickness of 3.5 nm, including a generalized Guinier-Porod contribution to capture the scattering contribution of apolipoproteins in the corona. The fit was performed using the SASfit software (50), with full details provided in *SI Appendix*. Note that the scattering intensity $I(q)$ measured at ESRF and EuXFEL exhibits good agreement, as shown in *SI Appendix*, Fig. S2. Hence, $I(q)$ obtained from ESRF was used for SAXS modeling due to the extended q-range, which provides improved resolution of structural features.

The $I(q)$ profiles of concentrated yolk-plasma samples were modeled using a soft-sphere structure factor, as shown in *SI Appendix*, Fig. S3 *B* and *C*. A repulsive $1/r^9$ potential was chosen to capture the finite deformability of LDL particles, describing the progressive increase in repulsion upon compression without interpenetration. Such soft-sphere models are broadly applied to deformable colloids and other systems that deviate from ideal hard-sphere interactions. The estimated $S(q)$ model fits of all concentrations are presented in Fig. 1*C* (the full $S(q)$ profiles are given in *SI Appendix*, Fig. S4). The structure factor peak position, q_m, shifts to lower q-values with decreasing LDL concentration, indicating an increase in the interparticle correlation distance $d_m = 2\pi/q_m$. As expected, the peak height of the structure factor, $S(q_m)$, increases with increasing LDL concentration (Table 1). The volume fractions ϕ obtained from the $S(q)$ fits are summarized in Table 1. The effective particle diameter of LDLs was determined using Boltzmann's hard-sphere criterion (*SI Appendix*, section 2.3). The corresponding effective volume fraction was then obtained by multiplying ϕ by a factor of 1.26.

Wave-Vector-Dependent Dynamics. To estimate the relaxation times of the LDL particles, we calculated the intensity autocorrelation functions $g_2(q, t)$ and modeled them using,

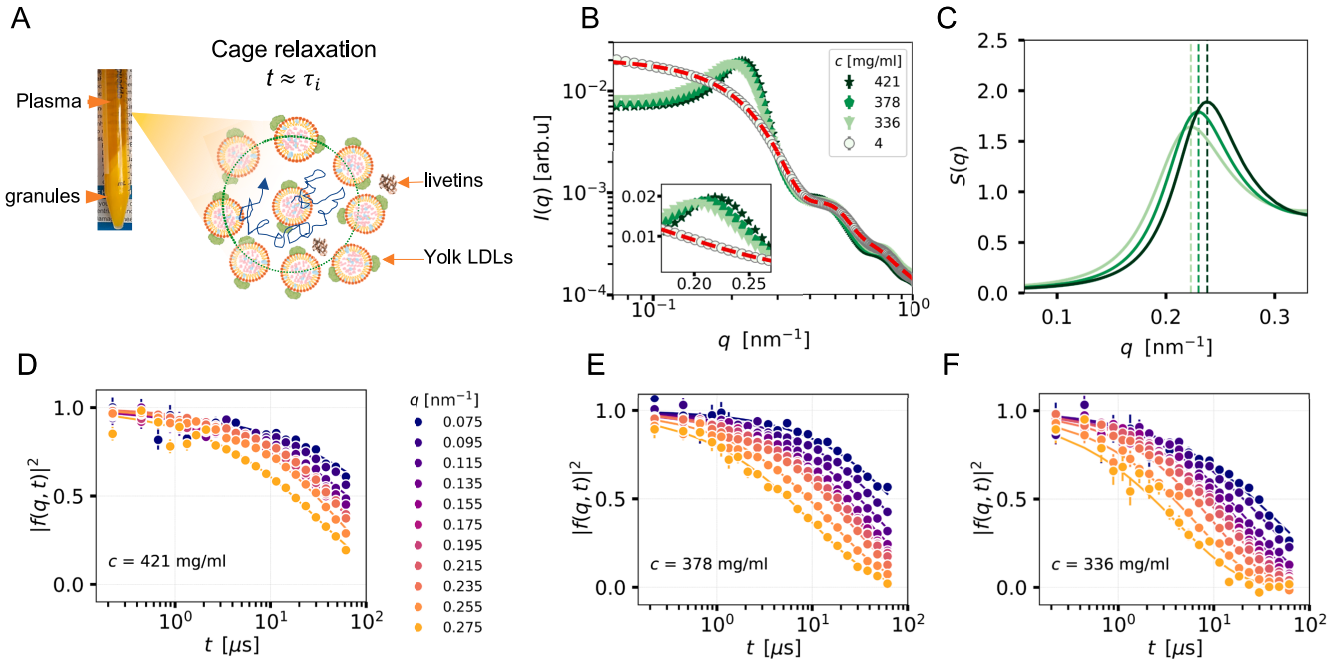

Fig. 1. Structure and dynamics of caged LDL particles. (*A*) The photo on the *Left* shows the two fractions of yolk: yolk-plasma (translucent) and yolk-granules (opaque), separated from egg yolk after centrifugation (*Materials and Methods*). The schematic on the *Right* indicates the cage relaxation of LDL molecules in yolk-plasma. The interaction time τ_i of LDL is ≈2.5 μs. (*B*) Normalized scattering intensity of egg yolk-plasma at different concentrations, obtained at ESRF. The red dashed line is the spherical core-shell fit to dilute $I(q)$ data ($c = 4$ mg/ml) with radius $R = 15.5$ nm, including generalized Guinier-Porod contribution (see *SI Appendix* for more details). A zoomed-in view around the structure factor peak q-regime is provided in the *Inset*. (*C*) The effective structure factor, $S(q)$, obtained by modeling the $I(q)$ as illustrated in *SI Appendix*, Fig. S3 *B–D*. $|f(q,t)|^2$ at different q values for (*D*) $c = 421$ mg/ml, (*E*) $c = 378$ mg/ml, and (*F*) $c = 336$ mg/ml. The solid lines indicate the fits using Eq. **1**.

$$g_2(q,t) = 1+\beta(q)|f(q,t)|^2 = 1+\beta(q)\,|\,\exp[-(t\,\tilde{\Gamma}(q))^{\alpha(q)}]\,|^2, \quad [1]$$

where $f(q,t)$ is the intermediate scattering function, $\tilde{\Gamma}(q)$ is the q-dependent relaxation rate, $\beta(q)$ is the speckle contrast, and $\alpha(q)$ is the Kohlrausch–Williams–Watts (KWW) exponent (51), describing the shape of the correlation function. In crowded or interacting systems, stretched exponential behavior ($\alpha(q) < 1$) at intermediate time scales is commonly associated with memory effects. Representative intermediate scattering functions and corresponding fits are shown in Fig. 1*D–F* (see *SI Appendix* for details on fitting). The intensity autocorrelation function $g_2(q,t)$ decays rapidly in the least crowded sample (Fig. 1*F*), indicating fast particle motion, whereas its slower decay at higher concentrations (Fig. 1*D* and *E*) reflects reduced mobility due to increased crowding and interparticle interactions. Additionally, we observe a pronounced stretching of the correlation functions with KWW exponents varying from 0.5 to 0.8 (*SI Appendix*, Fig. S6), indicating greater stretching (lower α) at higher concentrations. From the stretched correlation functions, we extract mean relaxation rates via $\Gamma(q) = \tilde{\Gamma}(q)\,\alpha(q)\,/\Gamma_f(1/\alpha(q))$, where Γ_f denotes the Gamma function (52, 53). The resulting $\Gamma(q)$ values are depicted in Fig. 2*A*, and we observe a decrease of $\Gamma(q)$ with increasing concentration, indicating a slowdown in the particle dynamics as expected. In all samples, we find a $\Gamma(q) \sim q^2$ (solid lines in Fig. 2*A*) behavior at low q values, which is typical of Brownian dynamics (54, 55). However, $\Gamma(q)$ significantly deviates from the Brownian behavior at q values near the structure factor peak at q_m. Such modulations in $\Gamma(q)$ around the q_m are typical signatures of collective relaxation phenomena (de Gennes narrowing: $\Gamma(q) \propto 1/S(q)$) observed in dense fluids, protein solutions, colloids, and glasses (19, 53, 56–58).

Next, we examine the wavevector-dependence of the KWW exponent α as shown in *SI Appendix*, Fig. S6. In all samples, the correlation functions display pronounced stretched-exponential relaxation, with $\alpha(q)$ in the range 0.5 to 0.8 and for $q < q_m$, α shows a weak decreasing trend with increasing concentration. In general, $\alpha < 1$ can arise from several mechanisms, including dynamical heterogeneity (59), memory effects associated with transient caging (60), local event dynamics (61), etc. In the present case, however, the α values exhibits an $S(q)$-like modulation near the structure-factor peak ($q > 0.15$ nm^{-1}), with the effect becoming more pronounced at the highest LDL concentration. This behavior points to pronounced memory effects in the LDL dynamics on time scales $t \gtrsim \tau_i$ (32, 60, 62), giving rise to a stretched-exponential decay of the intermediate scattering function $f(q,t)$ and consequently to $\alpha < 1$. Similar

Table 1. Details of sample and estimated quantities

c	YP_w	B_w	ϕ	q_m	$S(q_m)$	r_{cage}
[mg/ml]	[wt%]	[wt%]		[nm^{-1}]		nm
421	100	0	0.43	0.238	1.89	3.4 ± 0.1
378	90	10	0.4	0.23	1.79	5.1 ± 0.1
336	80	20	0.35	0.223	1.64	7.6 ± 0.8

YP_w: relative amount of yolk-plasma in solution.

B_w: relative amount of 170 mM NaCl solution added.

c denotes the mass of LDLs per unit final solution volume, ϕ denotes the volume fraction estimated from $S(q)$ modeling. q_m denotes the q-position of the maximum of the structure factor, $S(q_m)$ is the maximum value of the structure factor, and r_{cage} is the size of the cage deduced from the mean square displacement analysis described in *Discussion*.

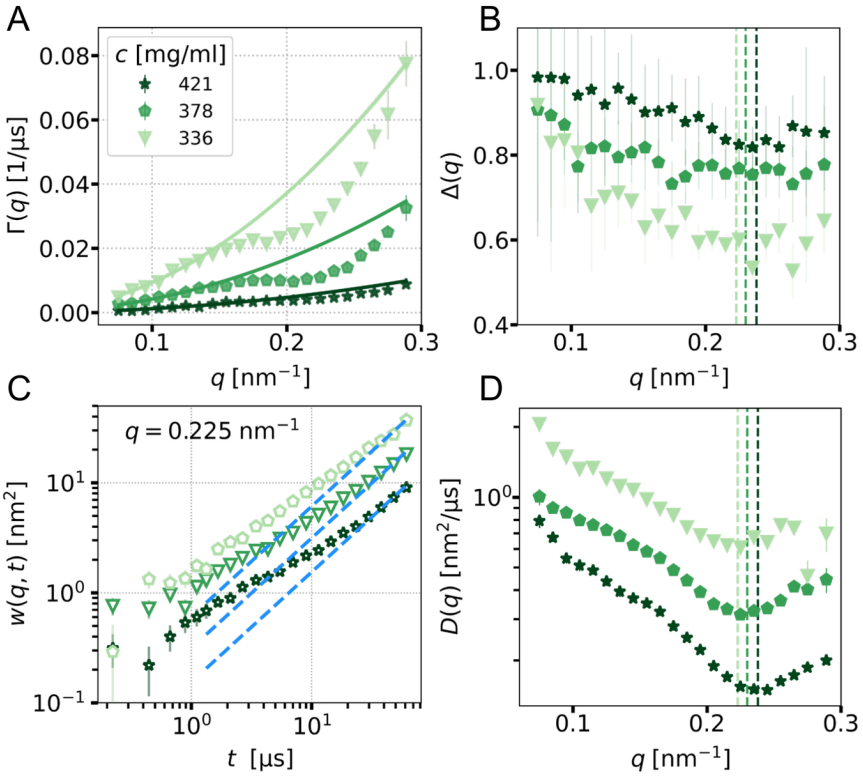

Fig. 2. Length-scale dependent dynamics of LDLs. (*A*) Wavevector-dependent relaxation rate of yolk-plasma at different concentrations. The solid line is the fit using $\Gamma(q) = \tilde{D}\, q^2$, performed at the first 6 data points (q-range of 0.075 to 0.125 nm^{-1}), where $\tilde{D}$ is a constant. The strong deviation of experimental data points at $q > 0.15$ nm^{-1} from the fit indicates the de Gennes narrowing. (*B*) The wavevector-dependent reduced memory function (or nonexponentiality function) of all samples. (*C*) Comparison of $w(q, t)$ of all samples at $q = 0.225\,\text{nm}^{-1}$. Blue dashed lines in (*C*) indicate linear fits at long-waiting times. (*D*) The diffusion coefficient extracted from the linear fit of $w(q, t)$. The dashed vertical lines in *B* and *D* indicate the peak position of the structure factor (q_m).

behavior has been observed in metallic glasses near the $S(q)$ peak (53, 63, 64).

This interpretation can be understood by considering *SI Appendix*, Eq. **S8**, which relates $f(q, t)$ to the collective memory function. In the short-time regime ($t \ll \tau_\text{i}$), the memory term (i.e., the integral involving $M_\text{c}(q, t)$) is negligible, resulting in an exponential decay of $f(q, t)$ (32). However, at longer times, the memory term becomes significant, capturing the influence of past particle configurations on current dynamics, a hallmark of caging. The degree of stretching in $f(q, t)$, and thus the deviation of α from unity, reflects the strength of these memory effects. A quantitative measure of this behavior is given by the reduced memory function (or nonexponentiality function), $\Delta(q)$ (Eq. **5**) (32, 60, 62). Weak and strong memory effects are characterized by $\Delta(q) = 0$ and $\Delta(q) = 1$, respectively. Fig. 2*B* shows the experimentally extracted reduced memory function for LDLs. Overall, $\Delta(q)$ increases with LDL concentration, indicating enhanced memory effects in denser suspensions. Additionally, in all samples, $\Delta(q)$ decreases with increasing q, and at the highest concentration, $\Delta(q)$ exhibits a local minimum near the $S(q)$ peak position. This feature is consistent with previous experimental observations and theoretical predictions based on mode-coupling approximations for moderately polydisperse colloidal suspensions (60, 65, 66).

Because the dynamics are subdiffusive at intermediate time scales, the diffusion coefficient cannot be directly extracted from the intermediate scattering function. Instead, we determined the collective width function, $w(q, t)$ (Eq. **9**), which becomes linear at the longest experimental times (Fig. 2*C*). Fitting this linear regime (dashed blue curves in Fig. 2*C*) yields the q-dependent long-time diffusion coefficient $D(q)$ from the slope of the fit (67). The estimated $D(q)$ values for all samples are plotted in Fig. 2*D*. The $D(q)$ exhibits a minimum at $q \approx q_\text{m}$, indicating that density fluctuations with wavelengths corresponding to the typical cage structures are slowed down relative to other modes. This behavior suggests a coupling to the local structure of the suspension.

Discussion

In the absence of hydrodynamic interactions, the wave-vector dependence of $D(q)$ would entirely result from the structural correlations, following the relation $D(q) = D_0/S(q)$ (68). However, comparison of $D_0/D(q)$ and $S(q)$ in *SI Appendix*, Fig. S8 reveals significant discrepancies in their q-dependence, indicating the presence of strong hydrodynamic interactions.

Given the lack of theoretical expressions for $D(q)$ valid on the interaction and long-time scale, we introduce an effective hydrodynamic function $H^*(q)$ to interpret our results. This function mirrors the familiar form for short-time dynamics (27, 69):

$$D(q) = \frac{D_0 H^*(q)}{S(q)}, \qquad [2]$$

where $H^*(q)$ captures hydrodynamic interactions on the long-time scales relevant to our experiment. It is related to the short-time hydrodynamic function by $H^*(q) = \frac{D_\text{s}^\text{long}}{D_\text{s}^\text{short}} H(q)$, where D_s^long and D_s^short are the long- and short-time self-diffusion coefficients, respectively. Rescaled hydrodynamic functions of

this kind have previously been employed to model data from hemoglobin solutions (28) and colloidal suspensions (70, 71). This approach enables us to extract $H^*(q)$ from experimental data using Eq. **2** (Fig. 3*A*). We find that the peak positions of $H^*(q)$ closely align with those of $S(q)$, as indicated by the vertical dashed lines in Fig. 3*A*. Moreover, the q-dependence of $H^*(q)$ is well captured by the $\delta\gamma$-formalism of Beenakker and Mazur (72, 73) (*Materials and Methods* and *SI Appendix*, Fig. S9). Comparable scaling behavior has been reported for colloids within restricted q-intervals (28), and more recently by us in dense ferritin solutions (30).

The large wave-vector limit of the short-time hydrodynamic function $H(q \to \infty)$, yields the normalized self-diffusion coefficient D_s^{short}/D_0 (27). Similarly, for the effective hydrodynamic function $H^*(q)$, the long-q limit gives $H^*(q \to \infty) = D_s^{\text{long}}/D_0$. We extract this quantity from our experimental data and plot D_s^{long}/D_0 as a function of ϕ_{eff} in *SI Appendix*, Fig. S11. In our recent study on ferritin (30), the long-time self-diffusion followed the predictions of the hard-sphere-based model by Medina-Noyola (74) and van Blaaderen et al. (75), in which direct and hydrodynamic interactions are decoupled. In this framework, hydrodynamic interactions influence only the short-time self-diffusion, while direct interactions are described through the contact value of the pair correlation function.

However, this model fails to account for the significantly reduced values of D_s^{long}/D_0 observed for LDL particles (*SI Appendix*, Fig. S12). This discrepancy arises from neglecting particle softness and long-range hydrodynamic interactions. These effects are incorporated in the theoretical treatment by Tokuyama et al. (37, 42), which provides an expression for the volume-fraction dependence of D_s^{long}/D_0 that includes both short- and long-range hydrodynamic interactions:

$$\frac{D_s^{\text{long}}}{D_0} = \frac{1-(9\phi/32)}{1+L(\phi)+\epsilon K(\phi)},$$
$$K(\phi) = \frac{(\phi/\phi_0)}{(1-\phi/\phi_0)^2} \qquad [3]$$

For a hard-sphere potential, $\epsilon = 1$, whereas for a soft repulsive interaction described by an inverse power-law potential, $U(r) = k_B T(\frac{\sigma}{r})^n$, ϵ is obtained from the fitting for $9 \leq n < 36$ (76), where σ denotes the effective particle diameter. The expression for $L(\phi)$ is provided in *Materials and Methods*. The parameter ϕ_0 represents a singular volume fraction which is determined by the many-body long-range hydrodynamic interactions between particles. The numerator term, $(9\phi/32)$, arises from the coupling between direct interactions and short-range hydrodynamic interactions. The function $K(\phi)$, which scales strongly with volume fraction, encapsulates many-body correlation effects due to long-range hydrodynamic interactions and is the primary contributor to the significant reduction in D_s^{long} (*SI Appendix*, Fig. S10) (36).

The prediction of D_s^{long}/D_0 for this model, assuming hard-sphere interactions (dotted line in *SI Appendix*, Fig. S11), do not align with the experimental values. In contrast, D_s^{long}/D_0 for soft-spheres aligns with the data (red line in *SI Appendix*, Fig. S11), highlighting the critical role of particle softness in limiting the self-diffusion coefficients of LDL particles in egg yolk-plasma. Note that $S(q)$ of LDL particles is modeled using an inverse power-law potential with $n = 9$, hence ϵ is treated as a fitting parameter (76). The estimated values from the soft-sphere fit given in Fig. 3*B*, are $\epsilon \approx 2.6$ and critical volume fraction, $\phi_0 \approx 0.66$. To facilitate a clearer comparison, the x-axis of *SI Appendix*, Fig. S11 was normalized by ϕ_0, enabling a direct comparison with the hard-sphere results (Fig. 3*B*). This normalization places both systems on a common relative scale that reflects their proximity to the dynamical arrest point. On this normalized scale, the diffusion coefficients of the LDLs are found to be ≈3 times lower than those of the hard-sphere system.

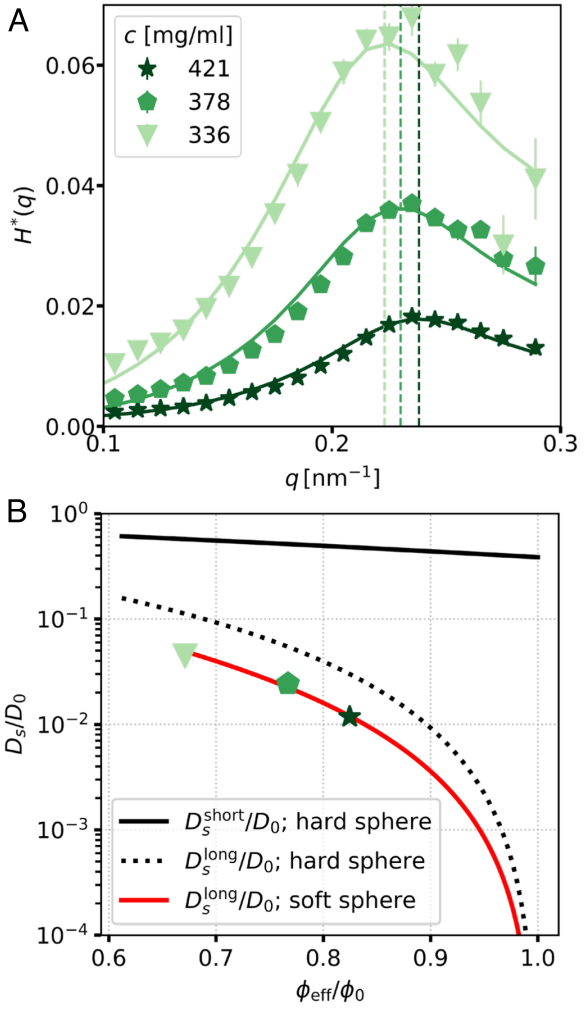

Fig. 3. Hydrodynamic interactions and normalized self-diffusion coefficient. (*A*) Experimental hydrodynamic functions (solid data points) along with model fits (solid line) as described in the text. Dashed vertical lines indicate the peak position of the experimental structure factor (q_m). (*B*) The self-diffusion coefficient of LDLs as a function of the normalized effective volume fraction of LDLs with respect to critical volume fraction from the soft-sphere fit, solid black curve: Eq. **8**, black dotted curve: Eq. **3** with $\epsilon = 1$, and solid red curve: Eq. **3** with $\epsilon \approx 2.6$ (obtained from fit).

Next, we examine the validity of the Stokes–Einstein relation by comparing the effective viscosity ($k_B T/6\pi R D_s^{\text{long}}$) estimated from XPCS with viscosity values obtained from rheology measurements in *SI Appendix*, Fig. S13. The shear-dependent viscosity is ≈2 to 3 times higher than that estimated from XPCS utilizing D_s^{long} values. This suggests that the decrease in diffusion coefficients observed at high concentrations (Fig. 3*B*) could not be scaled with the increase in macroscopic viscosity measured through rheometry. This behavior has previously also been observed in colloidal systems (25) and small organic compounds (26) at high concentrations near the glass transition. This decoupling of momentum and mass transport, and hence

deviations from the Stokes–Einstein relation, is a hallmark of dynamics approaching the glass transition (25).

Additional insight into the nature of the stretched correlation function can be obtained by evaluating the mean-square displacement (MSD) from the intermediate scattering function. In the short- and long-time regimes, a diffusive behavior (MSD $\sim t$) is expected, denoted by the blue dash-dotted and dashed lines (Fig. 4*A*). However, at time scales of τ_i, the MSD displays a subdiffusive regime with MSD $\sim t^{\zeta}$ ($\zeta < 1$). In other words, we observe a transition from short-time to long-time diffusive behavior on the experimentally investigated time scales. This nonlinear behavior of the MSD is in good agreement with the pronounced stretching of the correlation functions observed (*SI Appendix*, Fig. S6).

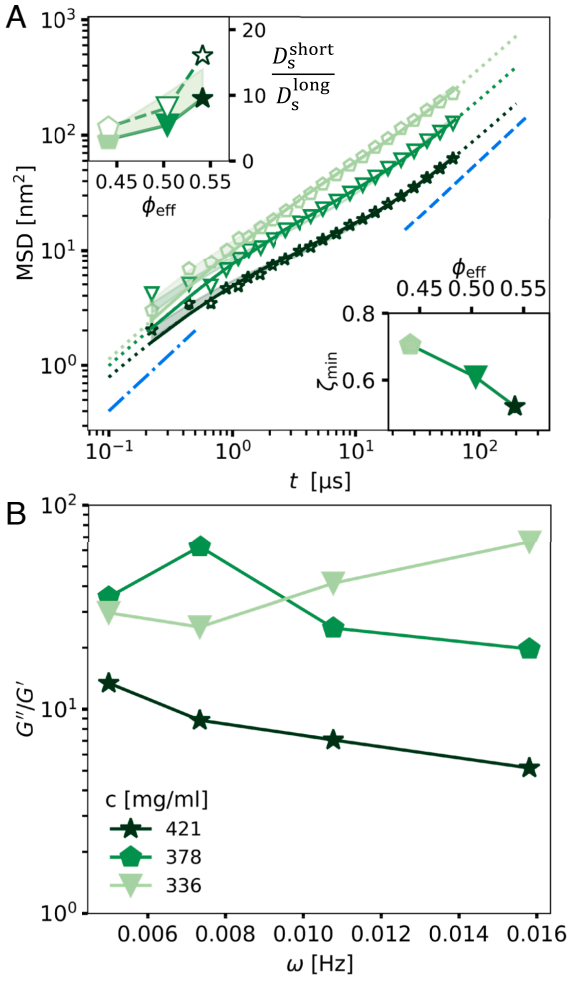

Fig. 4. Mean squared displacement and the loss-tangent. (*A*) Comparison of MSD of all samples. The solid curves are fits using Eq. **11**. The dotted curves are the extrapolation of the fits. The blue dash-dotted and dashed lines indicate MSD $\sim t$. These lines serve as a guide to the eye and indicate the short-time and long-time behavior of the MSD, respectively. To account for the limited data quality at short experimental time scales, we refitted the MSD data by adding and subtracting the experimental uncertainty, i.e., $y = \text{MSD} \pm \delta_{\text{MSD}}$. The resulting fits define the boundaries of the shaded region in (*A*). The *Inset* on the *Left* shows the ratio D_s^{short}/D_s^{long} obtained from the MSD fit (closed data points) and from $H^*(q)$ fit (open data points). Both perturbed MSD fits ($y = \text{MSD} \pm \delta_{\text{MSD}}$) yield larger D_s^{short}/D_s^{long} ratios, indicating an asymmetric (*Upper*) uncertainty bound. The *Inset* on the *Right* shows the minimum value of ζ as a function of effective volume fraction. (*B*) The loss-tangent as a function of frequency estimated from rheology measurements. Note that a loss-tangent greater than unity indicates that the sample is in a liquid state.

As the concentration increases, the MSD decreases, indicating the expected slowdown associated with crowding. Furthermore, the distinction between short- and long-time regimes becomes increasingly pronounced at higher concentrations. To quantify this effect, the MSD curves are modeled using Eq. **11**, and the corresponding D_s^{short}/D_s^{long} values are extracted and compared with that obtained from $H^*(q)$ fits (Fig. 3*A*) in the *Inset* of Fig. 4*A*. The ratio D_s^{short}/D_s^{long} derived from the MSD fits is ≈1.5 times lower than the corresponding values obtained from the $H^*(q)$ fits. This discrepancy likely arises from the limited time resolution of the MSD data at very short experimental times, where experimental noise hinders accurate determination of the initial diffusive regime and can lead to an underestimation of D_s^{short}. To account for the limited data quality at short times, we refitted the MSD by incorporating the experimental uncertainty–both adding and subtracting it (see *Materials and Methods* for details)–which provides the error bounds for the ratio D_s^{short}/D_s^{long}. Hence, within the experimental uncertainty, the values of D_s^{short}/D_s^{long} estimated from the MSD and $H^*(q)$ fits are in good agreement. Moreover, the MSD analysis assumes a hard-sphere model, whereas LDL particles are soft and deformable. A quantitative framework that explicitly accounts for softness and viscoelastic interactions would be required to reconcile the two estimates of D_s^{short}/D_s^{long}, however, such models are, to our knowledge, not yet available for LDL-like systems. At the highest concentration, the diffusion coefficient differs by a factor of ≈10. This value is close to that of monodisperse colloids near freezing (35, 77), which suggests the LDLs are packed very densely. This dense packing serves two primary biological functions: it maximizes the storage of vital lipids for the developing embryo and helps maintain the structural integrity of the yolk. Despite the marked reduction in diffusion rates, the yolk remains in a liquid state (loss-tangent > 1 in Fig. 4*B*), indicating a "sluggish liquid" phase. This condition is potentially optimal for biological purposes—stable enough to preserve lipid storage while remaining fluid enough for nutrient access by the embryo when required.

More information on the caged motion at intermediate time scales can be obtained by extracting the anomalous exponent $\zeta = \frac{d\ln(\text{MSD}(t))}{d\ln(t)}$. The ζ-values estimated from the MSD fit for all samples are displayed in *SI Appendix*, Fig. S15. As the volume fraction increases, ζ decreases, indicating a stronger degree of subdiffusive behavior due to crowding and interactions. The strength of this caging effect is quantified by the minimum ζ value observed within the measurement time window, as shown in the *Inset* of Fig. 4*A*. As expected, the caging strength increases with volume fraction, indicated by a reduction in ζ_{min}, highlighting the impact of crowding on the motion of soft LDL particles. The cage size, defined as $r_{cage} \approx \sqrt{\text{MSD}(t = t_{cage})}$, is estimated from the MSD at the cage rearrangement time t_{cage}-the point where the MSD starts to rise from its plateau (78). This plateau corresponds to the minimum ζ values, making it a good reference for determining r_{cage} (Table 1). With increasing volume fraction, r_{cage}/R decreases, reflecting enhanced local confinement and reduced amplitude of particle rattling within the cages (78).

Summary

In summary, we employed MHz-XPCS on native yolk-plasma to probe LDL dynamics on microsecond time scales–a regime typically inaccessible in protein systems. Within this time window, we directly captured particle rattling, memory effects, and the onset of collective relaxation on nanometer length scales. LDLs exhibit stretched correlation functions and subdiffusive dynamics at intermediate times, arising from both direct interactions and long-range hydrodynamic coupling. We quantified these memory effects in a wavevector-resolved manner: The reduced memory function $\Delta(q)$ and the collective relaxation rate both show pronounced minima at $q \approx q_m$, linking the dynamical slowdown to the cage-scale structure. We further introduced an effective hydrodynamic function $H^*(q)$, demonstrating that hydrodynamic interactions continue to shape collective motion well beyond the nominal short-time limit.

At the highest concentration, the long-time self-diffusion is slowed by nearly two orders of magnitude compared with dilute solutions. In addition, the long-time self-diffusion is a factor of three lower than the hard-sphere predictions when normalized to the critical volume fraction. This suppression is captured by a soft-sphere transport relation with an effective softness parameter and apparent arrest volume fraction. At physiological concentrations, LDL yolk-plasma behaves as a densely packed, "sluggish liquid", exhibiting a pronounced decoupling between short- and long-time diffusion ($D_s^{short}/D_s^{long} \approx 10$). This state stabilizes the LDL-rich yolk while maintaining the controlled mobility required for lipid release during embryonic development.

More broadly, the combined analysis of $\Delta(q)$, $\Gamma(q)$, and $H^*(q)$, together with the soft-sphere transport (ϵ, ϕ_0), establishes a quantitative framework for crowded protein systems. It links cage-scale structure, memory effects, and long-time diffusivity-offering a broadly applicable framework for understanding relaxation and transport in dense biological fluids such as protein solutions, condensates, cytoplasm, and other soft-matter systems.

Materials and Methods

Sample Preparation. The egg yolk used in this study was obtained from a hen egg purchased at a supermarket. The yolk extracted from the egg was centrifuged (44) at 7,197 g for ≈4 d to separate the yolk-plasma from the yolk-granules (see *SI Appendix* for details). During centrifugation, the heavier entities in the yolk (called yolk-granules) settled, leaving behind a yellow-translucent liquid known as egg yolk-plasma (Fig. 1*A*). The total dry mass content of the yolk-plasma was determined by complete water removal (dried under fume hood) and subsequent weighing of the residue, yielding a value of 49 wt%. Based on prior compositional analyses, LDLs account for approximately 85 wt% of the dry matter (44), indicating that undiluted yolk-plasma contains ≈421 mg/ml of LDLs. To prepare samples of lower LDL concentration, the yolk-plasma was diluted to 90 wt% and 80 wt% using NaCl buffer (170 mM), resulting in final LDL concentrations of 378 mg/ml and 336 mg/ml, respectively. The exact amounts of buffer added for each dilution are listed in Table 1. All samples were stored at 5 °C until use. For XPCS measurements, the yolk-plasma solutions were loaded into 1.5 mm-diameter quartz capillaries and vacuum-sealed with epoxy glue. All XPCS experiments were conducted at a temperature of 25 °C.

Estimation of $I(q)$. The scattering intensity provided in this work, $I(q) = I_{raw}(q) - I_{water}(q)$, where $I_{raw}(q)$ and $I_{water}(q)$ are the scattering intensities of sample and water, respectively, were obtained by azimuthal integration of the scattering pattern from the 2D detector. In yolk-plasma, the LDLs are dispersed in water, hence, the water background is subtracted to get the scattering contribution of LDLs. Normalization of $I(q)$ is performed such that the high-q scattering intensities of higher concentrations are made to coincide with those of the $c = 4$ mg/ml sample.

Estimation of D_0^d and D_0. The diffusion coefficient of LDL particles in the dilute limit is estimated by the Stokes–Einstein relation,

$$D_0^d = \frac{k_B T}{6\pi\eta R}, \quad [4]$$

where $T = 298$ K, η and $R = 15.5$ nm are the temperature of the system, viscosity of water, and radius of the LDL particles in dilute solution, respectively. However, D_0 is the effective diffusion coefficient of LDL particles in dilute solution estimated using the Stokes–Einstein relation, considering the effective radius of LDL particles at different concentrations (*SI Appendix*, Fig. S3 *B–D*).

Reduced Memory Function. Reduced memory function (or nonexponentiality function) (32, 60, 62) is given by

$$\Delta(q) = 1 - \frac{\Gamma(q)}{\Gamma^s(q)}, \quad [5]$$

where $\Gamma^s(q)$ denotes the relaxation rate in the short-time limit $t \ll \tau_i$ during which $f(q, t)$ decays exponentially (32). To estimate $\Gamma^s(q)$, Eq. **1** was fitted to the data with $\alpha = 1$ for $t < \tau_i$ (see *SI Appendix* for details on the extraction procedure).

Hydrodynamic Function. The short-time hydrodynamic function can be decomposed into a self-part $\frac{D_s^{short}}{D_0}$ and a q-dependent part $H_d(q)$ using,

$$H(q) = \frac{D_s^{short}}{D_0} + H_d(q), \quad [6]$$

where D_s^{short} is the self-diffusion coefficient and the q-dependent part of hydrodynamic function $H_d(q)$ is given by ref. 27,

$$H_d(q) = \frac{3}{2\pi}\int_0^\infty \left(\frac{\sin(Rq')}{(Rq')}\right)^2 \frac{1}{1+\phi S_\gamma(Rq')}\, d(Rq') \times \int_{-1}^{1} dx(1-x^2)[S(|q-q'|)-1], \quad [7]$$

where x is the cosine of the angle between the wave vectors q and q' and S_γ is a known function independent of particle correlation and is given in ref. 79. For $q \to \infty$, $H_d(q)$ goes to zero and $H(q)$ becomes the normalized short-time translational self-diffusion coefficient $\frac{D_s^{short}}{D_0}$. The q-dependent part $H_d(q)$ was estimated using the Jscatter (80) Python library, where the structure factor of the samples was given as input.

Theoretical Predictions of D_s^{short}/D_0. The theoretical prediction of $\frac{D_s^{short}}{D_0}$ by M. Tokuyama and I. Oppenheim (37), incorporating both short-range and long-range hydrodynamic interactions and their coupling, is given by,

$$\frac{D_s^{short}}{D_0} = \frac{1}{1+L(\phi)}$$

$$L(\phi) = \frac{2b_f^2}{1-b_f} - \frac{c_f}{1+2c_f} + \left[-\frac{2b_f c_f}{1-b_f+c_f}\left(1 - \frac{6b_f c_f}{1-b_f+c_f+4b_f c_f} + \frac{2b_f c_f}{1-b_f+c_f+2b_f c_f}\right) + \frac{b_f c_f^2}{(1+c_f)(1-b_f+c_f)}\left(1 + \frac{3b_f c_f^2}{(1+c_f)(1-b_f+c_f)-2b_f c_f^2} - \frac{b_f c_f^2}{(1+c_f)(1-b_f+c_f)-b_f c_f^2}\right)\right]$$

$$b_f = (9\phi/8)^{1/2},\ c_f = 11\phi/6 \quad [8]$$

The first, second, and third terms in $L(\phi)$ correspond to contributions from the long-range hydrodynamic interaction, short-range hydrodynamic interaction, and their coupling, respectively (37).

Extraction and Modeling of MSD. The collective width function, $w(q, t)$ is extracted from $f(q, t)$ using (81, 82),

$$w(q, t) = -\frac{1}{q^2} \ln[f(q, t)]. \quad [9]$$

The incoherent MSD can then be estimated from $w(q, t)$ for $qR \geq 2.5$ using the relation (67, 81, 83)

$$\text{MSD}(t) = 6\, w(q, t) \frac{D_s^{\text{long}}}{D(q)}, \quad [10]$$

which is an empirical expression from experiments (67, 83). The validity of this expression for yolk-plasma solutions is confirmed by the collapse of all MSD curves for $qR \geq 2.5$ as shown in *SI Appendix*, Fig. S14. Thus, averaging all MSD values displayed in *SI Appendix*, Fig. S14 yields a single representative MSD curve for each sample, as shown in Fig. 4*A*. An expression to MSD for concentrated, equilibrium suspensions of hard-spheres is given by Tokuyama et al. (84, 85),

$$\text{MSD}(t) = \frac{1}{\nu} \ln\left[1 + \frac{D_s^{\text{short}}}{D_s^{\text{long}}} \exp\left(6\nu D_s^{\text{long}} t\right)\right], \quad [11]$$

where ν is a free parameter to be determined and is related to the static properties in the equilibrium suspension (84).

Furthermore, to account for the limited data quality at short experimental time scales, we refitted the MSD data by adding and subtracting the experimental uncertainty, i.e., $y = \text{MSD} \pm \delta_{\text{MSD}}$, using Eq. **11**. Both perturbed fits yielded larger $D_s^{\text{short}}/D_s^{\text{long}}$ ratios than the original fit, indicating that the uncertainty predominantly affects the upper side of the fitted parameters. Accordingly, the uncertainty in $D_s^{\text{short}}/D_s^{\text{long}}$ is asymmetric and is reported as a one-sided (upper) bound, as shown in the *Inset* of Fig. 4*A*.

X-Ray Experimental Parameters. XPCS measurements were conducted at the MID instrument (43) of the EuXFEL in a SAXS configuration. The experiments utilized the full self-amplified spontaneous emission (SASE) with a mean photon energy of 10 keV and a focused beam size of 11.7 ± 0.3 μm. The EuXFEL delivers X-ray pulse trains at a repetition rate of 10 Hz. Each train in the experiment contained 310 individual pulses with an intratrain repetition rate of 4.5 MHz, corresponding to a pulse spacing of 222 ns. Scattered X-rays were recorded using the Adaptive Gain Integrating Pixel Detector (AGIPD), featuring a pixel size of 200 μm and positioned 7.68 m downstream from the sample. The primary dataset was acquired during experiment number 5397, while additional supporting data were collected during experiment 6996, which employed slightly different beam parameters. Full details of both experimental configurations are provided in *SI Appendix*. The datasets were analyzed using the dedicated data processing pipeline developed by EuXFEL (86). X-ray beam-induced effects (45, 48) and mitigation strategies are detailed in *SI Appendix*. The yolk-plasma was found to be stable until a critical dose of 20 kGy, and hence all measurements shown in this manuscript were performed below the critical threshold of 20 kGy using a dose rate of 0.23 kGy/μs. The SAXS experimental parameters at ESRF (beamline ID02) are provided in *SI Appendix*, Table S3.

Data, Materials, and Software Availability. Data recorded for the experiment at the European XFEL are available at (DOI: 10.22003/XFEL.EU-DATA-005397-00 and 10.22003/XFEL.EU-DATA-006996-00) (87, 88). Data recorded at ESRF are available at (DOI: 10.15151/ESRF-ES-2009918726) (89).

ACKNOWLEDGMENTS. We acknowledge European XFEL in Schenefeld, Germany, for the provision of X-ray free-electron laser beamtime at the Scientific Instrument MID (Materials Imaging and Dynamics) and would like to thank the staff for their assistance. The data presented here were taken as part of the beamtimes with experiment numbers 5397 and 6996. We acknowledge the participation of Marvin Kowalski, Mohammad Sayed Akhundzadeh, Jenny Schrage, Pia Kwiasowski, Maximilian Senft, Lara Reichart, and Chang Hee Woo during the EuXFEL beamtime. We thank the European Synchrotron Radiation Facility (ESRF) for the provision of synchrotron radiation facilities at TRUSAXS instrument (Time Resolved Ultra Small Angle X-ray Scattering), ID02 (SC-5435), with additional support from Theyencheri Narayanan. We acknowledge the participation of Randeer Gautam, Moritz Puritscher, Fabian Prandl, Lovisa Jansson, Milla Åhlfeldt, and Sampad Bag during the ESRF beamtime. We acknowledge financial support by the consortium DAPHNE4NFDI in association with the German National Research Data Infrastructure (NFDI) e.V.–project number 4602487. This work was supported through the Maxwell computational resources operated at Deutsches Elektronen-Synchrotron DESY, Hamburg, Germany. We acknowledge Dr. D. C. F. Wieland for providing access to the Bolin Gemini rotational HR nano-rheometer for rheology measurements. M.P. thanks the DELTA machine group for providing synchrotron radiation for sample characterization. We acknowledge BMBF (05K19PS1, 05K20PSA, and 05K22PS1) (to C.G.); 05K19VTB, (to F.Z. and F.S.), DFG-ANR (SCHR700/28-1, SCHR700/42-1, and ANR-16-CE92-0009) (to F.Z. and F.S.). C.G. acknowledges funding from NFDI 40/1 (DAPHNE4NFDI). A.G., I.A., and F.P. acknowledge funding from the European Union's Horizon Europe research and innovation programme under the Marie Skłodowska-Curie grant agreement No. 101081419 (PRISMAS) (I.A. and F.P.) and 101149230 (CRYSTAL-X) (A.G. and F.P.). F.P. acknowledges financial support by the Swedish National Research Council (Vetenskapsrådet) under Grant No. 2019-05542, 2023-05339 and within the Röntgen-Ångström Cluster Grant No. 2019-06075, and the kind financial support from Knut och Alice Wallenberg foundation (WAF, Grant No. 2023.0052). This research is supported by the Center of Molecular Water Science (CMWS) of DESY in an Early Science Project, the MaxWater initiative of the Max-Planck-Gesellschaft, Carl Tryggers (Project No. CTS 21:1589), and the Wenner-Gren Foundations (Project No. UPD2021-0144).

Author affiliations: [a]Department Physik, Universität Siegen, 57072 Siegen, Germany; [b]Deutsches Elektronen-Synchrotron DESY, 22607 Hamburg, Germany; [c]Department of Physics, AlbaNova University Center, Stockholm University, 10691 Stockholm, Sweden; [d]Institut für Angewandte Physik, Universität Tübingen, 72076 Tübingen, Germany; [e]European X-Ray Free-Electron Laser Facility, 22869 Schenefeld, Germany; [f]Institute for Biochemistry and Molecular Biology, Deutsches Elektronen-Synchrotron, 22607 Hamburg, Germany; [g]The Hamburg Centre for Ultrafast Imaging, 22761 Hamburg, Germany; [h]ESRF-The European Synchrotron, 38042 Grenoble, France; and [i]Fakultät Physik/ Dortmunder Elektronenspeicherringanlage, Technical University of Dortmund, 44221 Dortmund, Germany

Author contributions: N.D.A., M.D., F.P., F.S., and C.G. designed research; N.D.A., M.D., S.T., A.G., S.R., J.M., W.J., A.M.R., A.L., J.W., F.U., M.B., P.P.R., I.A., W.C., J.H., A.R.-F., J.-E.P., U.B., M.Y., R.S., R.R., A.M., F.L., M.P., F.Z., F.P., F.S., and C.G. performed research; N.D.A. and M.D. prepared and handled the samples; N.D.A. analyzed data; J.M., A.L., J.W., and F.B. provided the MID data analysis pipeline at European X-ray Free Electron Laser Facility; J.M., W.J., A.L., J.H., A.R.-F., J.-E.P., U.B., M.Y., R.S., R.R., and A.M. operated the Materials Imaging and Dynamics instrument at European X-ray Free Electron Laser Facility; W.C. operated the ID02 beamline at European Synchrotron Radiation Facility and provided the data analysis pipeline; N.D.A., M.D., S.T., A.G., S.R., J.M., W.J., A.M.R., A.L., J.W., F.U., M.B., P.P.R., I.A., W.C., J.H., A.R.-F., J.-E.P., F.B., U.B., M.Y., R.S., R.R., A.M., F.L., M.P., F.Z., F.P., F.S., and C.G provided input for the paper; and N.D.A. and C.G. wrote the paper.

1. J. W. Gofman *et al*., The role of lipids and lipoproteins in atherosclerosis. *Science* **111**, 166–186 (1950).
2. A. Saari, W. Powrie, O. Fennema, Isolation and characterization of low-density lipoproteins in native egg yolk plasma. *J. Food Sci.* **29**, 307–315 (1964).
3. T. Li, Y. Jin, J. Wu, Z. Ren, Beyond energy provider: Multifunction of lipid droplets in embryonic development. *Biol. Res.* **56**, 38 (2023).
4. B. A. Ference, E. Braunwald, A. L. Catapano, The LDL cumulative exposure hypothesis: Evidence and practical applications. *Nat. Rev. Cardiol.* **21**, 701–716 (2024).
5. H. J. Carpenter, M. H. Ghayesh, A. C. Zander, P. J. Psaltis, "Effect of nonlinear blood viscosity on LDL transport and fluid-structure interaction biomechanics of a multi-stenosis left circumflex coronary artery" in *Advances in Nonlinear Dynamics: Proceedings of the Second International Nonlinear Dynamics Conference (NODYCON 2021), Volume 1*, W. Lacarbonara et al., Eds. (Springer, 2022), pp. 39–48.
6. C. Zhu, Y. Xia, Biomimetics: Reconstitution of low-density lipoprotein for targeted drug delivery and related theranostic applications. *Chem. Soc. Rev.* **46**, 7668–7682 (2017).

7. C. Wang *et al*., Transporting mitochondrion-targeting photosensitizers into cancer cells by low-density lipoproteins for fluorescence-feedback photodynamic therapy. *Nanoscale* **13**, 1195–1205 (2021).
8. A. Jutkova, D. Chorvat, P. Miskovsky, D. Jancura, S. Datta, Encapsulation of anticancer drug curcumin and co-loading with photosensitizer hypericin into lipoproteins investigated by fluorescence resonance energy transfer. *Int. J. Pharm.* **564**, 369–378 (2019).
9. L. Dai *et al*., Low-density lipoprotein: A versatile nanoscale platform for targeted delivery. *Nanoscale Adv.* **5**, 1011–1022 (2023).
10. Y. L. Sun, B. Q. Ge, M. Z. Li, L. Wang, Z. X. Chen, The effect of macromolecular crowding degree on the self-assembly of fatty acid and lipid hydrolysis. *NPJ Sci. Food.* **7**, 39 (2023).
11. G. Nettesheim *et al*., Macromolecular crowding acts as a physical regulator of intracellular transport. *Nat. Phys.* **16**, 1144–1151 (2020).
12. B. Alric, C. Formosa-Dague, E. Dague, L. J. Holt, M. Delarue, Macromolecular crowding limits growth under pressure. *Nat. Phys.* **18**, 411–416 (2022).
13. M. Grimaldo, F. Roosen-Runge, F. Zhang, F. Schreiber, T. Seydel, Dynamics of proteins in solution. *Q. Rev. Biophys.* **52**, e7 (2019).
14. A. Girelli *et al*., Microscopic dynamics of liquid-liquid phase separation and domain coarsening in a protein solution revealed by x-ray photon correlation spectroscopy. *Phys. Rev. Lett.* **126**, 138004 (2021).
15. N. D. Anthuparambil *et al*., Salt induced slowdown of kinetics and dynamics during thermal gelation of egg-yolk. *J. Chem. Phys.* **161**, 055102 (2024).
16. R. Ramalingam, G. Jiang, H. Larjava, L. Häkkinen, Macromolecular crowding regulates matrix composition and gene expression in human gingival fibroblast cultures. *Sci. Rep.* **13**, 2047 (2023).
17. S. Bucciarelli *et al*., Dramatic influence of patchy attractions on short-time protein diffusion under crowded conditions. *Sci. Adv.* **2**, e1601432 (2016).
18. G. Nawrocki, IYu. Ph Wang, Y. Sugita, M. Feig, Slow-down in diffusion in crowded protein solutions correlates with transient cluster formation. *J. Phys. Chem. B* **121**, 11072–11084 (2017).
19. M. K. Braun *et al*., Crowding-controlled cluster size in concentrated aqueous protein solutions: Structure, self-and collective diffusion. *J. Phys. Chem. Lett.* **8**, 2590–2596 (2017).
20. D. Lavalette, C. Tétreau, M. Tourbez, Y. Blouquit, Microscopic viscosity and rotational diffusion of proteins in a macromolecular environment. *Biophys. J.* **76**, 2744–2751 (1999).
21. F. Zosel, A. Soranno, K. J. Buholzer, D. Nettels, B. Schuler, Depletion interactions modulate the binding between disordered proteins in crowded environments. *Proc. Natl. Acad. Sci. U.S.A.* **117**, 13480–13489 (2020).
22. M. Heinen *et al*., Viscosity and diffusion: Crowding and salt effects in protein solutions. *Soft Matter* **8**, 1404–1419 (2012).
23. M. Grimaldo *et al*., Protein short-time diffusion in a naturally crowded environment. *J. Phys. Chem. Lett.* **10**, 1709–1715 (2019).
24. C. Beck *et al*., Short-time transport properties of bidisperse suspensions of immunoglobulins and serum albumins consistent with a colloid physics picture. *J. Phys. Chem. B.* **126**, 7400–7408 (2022).
25. D. Bonn, W. K. Kegel, Stokes-Einstein relations and the fluctuation-dissipation theorem in a supercooled colloidal fluid. *J. Chem. Phys.* **118**, 2005–2009 (2003).
26. S. F. Swallen, M. Ediger, Self-diffusion of the amorphous pharmaceutical indomethacin near Tg. *Soft Matter* **7**, 10339–10344 (2011).
27. G. Nägele, On the dynamics and structure of charge-stabilized suspensions. *Phys. Rep.* **272**, 215–372 (1996).
28. W. Doster, S. Longeville, Microscopic diffusion and hydrodynamic interactions of hemoglobin in red blood cells. *Biophys. J.* **93**, 1360–1368 (2007).
29. F. Roosen-Runge *et al*., Protein self-diffusion in crowded solutions. *Proc. Natl. Acad. Sci. U.S.A.* **108**, 11815–11820 (2011).
30. A. Girelli *et al*., Coherent x-rays reveal anomalous molecular diffusion and cage effects in crowded protein solutions. *Nat. Commun.* **16**, 10814 (2025).
31. M. Dargasz *et al*., Depletion-induced interactions modulate nanoscale protein diffusion in polymeric crowder solutions. arXiv [Preprint] (2025). http://arxiv.org/abs/2509.04087v2 (Accessed 9 September 2025).
32. G. Nägele, P. Baur, R. Klein, Non-exponential relaxation of density fluctuations in strongly interacting colloidal suspensions. *Phys. A Stat. Mech. Appl.* **231**, 49–61 (1996).
33. T. Ando, E. Chow, J. Skolnick, Dynamic simulation of concentrated macromolecular solutions with screened long-range hydrodynamic interactions: Algorithm and limitations. *J. Chem. Phys.* **139**, 121922 (2013).
34. J. F. Brady *et al*., Stokesian dynamics. *Annu. Rev. Fluid Mech.* **20**, 111–157 (1988).
35. P. Holmqvist, G. Nägele, Long-time dynamics of concentrated charge-stabilized colloids. *Phys. Rev. Lett.* **104**, 058301 (2010).
36. M. Tokuyama, I. Oppenheim, Dynamics of hard-sphere suspensions. *Phys. Rev. E* **50**, R16–R19 (1994).
37. M. Tokuyama, I. Oppenheim, On the theory of concentrated hard-sphere suspensions. *Phys. A Stat. Mech. Appl.* **216**, 85–119 (1995).
38. G. Foffi *et al*., Hard sphere-like glass transition in eye lens α-crystallin solutions. *Proc. Natl. Acad. Sci. U.S.A.* **111**, 16748–16753 (2014).
39. P. Vodnala *et al*., Hard-sphere-like dynamics in highly concentrated alpha-crystallin suspensions. *Phys. Rev. E* **97**, 020601 (2018).
40. A. Stradner, P. Schurtenberger, Potential and limits of a colloid approach to protein solutions. *Soft Matter* **16**, 307–323 (2020).
41. J. Balbo, P. Mereghetti, D. P. Herten, R. C. Wade, The shape of protein crowders is a major determinant of protein diffusion. *Biophys. J.* **104**, 1576–1584 (2013).
42. M. Tokuyama, T. Moriki, Y. Kimura, Self-diffusion of biomolecules in solution. *Phys. Rev. E* **83**, 051402 (2011).
43. A. Madsen *et al*., Materials imaging and dynamics (mid) instrument at the European x-ray free-electron laser facility. *J. Synchrotron Rad.* **28**, 637–649 (2021).
44. M. Anton, Egg yolk: Structures, functionalities and processes. *J. Sci. Food Agric.* **93**, 2871–2880 (2013).
45. M. Reiser *et al*., Resolving molecular diffusion and aggregation of antibody proteins with megahertz X-ray free-electron laser pulses. *Nat. Commun.* **13**, 2041–1723 (2022).
46. F. Lehmkühler *et al*., Emergence of anomalous dynamics in soft matter probed at the European XFEL. *Proc. Natl. Acad. Sci. U.S.A.* **117**, 24110–24116 (2020).
47. N. D. Anthuparambil *et al*., Exploring non-equilibrium processes and spatio-temporal scaling laws in heated egg yolk using coherent x-rays. *Nat. Commun.* **14**, 5580 (2023).
48. Y. Chushkin *et al*., Probing cage relaxation in concentrated protein solutions by x-ray photon correlation spectroscopy. *Phys. Rev. Lett.* **129**, 238001 (2022).
49. N. Begam *et al*., Kinetics of network formation and heterogeneous dynamics of an egg white gel revealed by coherent x-ray scattering. *Phys. Rev. Lett.* **126**, 098001 (2021).
50. I. Breßler, J. Kohlbrecher, A. F. Thünemann, Sasfit: A tool for small-angle scattering data analysis using a library of analytical expressions. *J. Appl. Cryst.* **48**, 1587–1598 (2015).
51. G. Williams, D. C. Watts, Non-symmetrical dielectric relaxation behaviour arising from a simple empirical decay function. *Trans. Faraday Soc.* **66**, 80–85 (1970).
52. A. Arbe, J. Colmenero, Characterization of the "simple-liquid" state in a polymeric system: Coherent and incoherent scattering functions. *Phys. Rev. E* **80**, 041805 (2009).
53. B. Ruta *et al*., Wave-vector dependence of the dynamics in supercooled metallic liquids. *Phys. Rev. Lett.* **125**, 055701 (2020).
54. H. Srinivasan, V. K. Sharma, S. Mitra, Breaking the Brownian barrier: Models and manifestations of molecular diffusion in complex fluids. *Phys. Chem. Chem. Phys.* **26**, 29227–29250 (2024).
55. R. Metzler, J. H. Jeon, A. G. Cherstvy, E. Barkai, Anomalous diffusion models and their properties: Non-stationarity, non-ergodicity, and ageing at the centenary of single particle tracking. *Phys. Chem. Chem. Phys.* **16**, 24128–24164 (2014).
56. L. Hong, N. Smolin, J. C. Smith, De Gennes narrowing describes the relative motion of protein domains. *Phys. Rev. Lett.* **112**, 158102 (2014).
57. K. Nygård *et al*., Anisotropic de Gennes narrowing in confined fluids. *Phys. Rev. Lett.* **116**, 167801 (2016).
58. C. Caronna, Y. Chushkin, A. Madsen, A. Cupane, Dynamics of nanoparticles in a supercooled liquid. *Phys. Rev. Lett.* **100**, 055702 (2008).
59. A. Zaccone, Relaxation and vibrational properties in metal alloys and other disordered systems. *J. Phys. Condens. Matter* **32**, 203001 (2020).
60. P. Baur, G. Nägele, R. Klein, Nonexponential relaxation of density fluctuations in charge-stabilized colloids. *Phys. Rev. E* **53**, 6224–6237 (1996).
61. K. Trachenko, A. Zaccone, Slow stretched-exponential and fast compressed-exponential relaxation from local event dynamics. *J. Phys. Condens. Matter* **33**, 315101 (2021).
62. R. Klein, W. Hess, Mass-diffusion and self-diffusion properties in systems of strongly charged spherical particles. *Faraday Discuss. Chem. Soc.* **76**, 137–150 (1983).
63. N. Neuber *et al*., Disentangling structural and kinetic components of the α-relaxation in supercooled metallic liquids. *Commun. Phys.* **5**, 316 (2022).
64. P. Luo *et al*., Q-dependent collective relaxation dynamics of glass-forming liquid $Ca_{0.4}K_{0.6}(NO_3)_{1.4}$ investigated by wide-angle neutron spin-echo. *Nat. Commun.* **13**, 2092 (2022).
65. T. W. Taylor, B. J. Ackerson, Memory function for a colloidal liquid. *J. Chem. Phys.* **83**, 2441–2446 (1985).
66. W. Härtl, H. Versmold, U. Wittig, P. Linse, Structure and dynamics of polymer colloid suspensions from dynamic light scattering and Brownian dynamics simulation. *J. Chem. Phys.* **97**, 7797–7804 (1992).
67. P. Segre, P. N. Pusey, Dynamics and scaling in hard-sphere colloidal suspensions. *Phys. A Stat. Mech. Appl.* **235**, 9–18 (1997).
68. W. Hess, R. Klein, Generalized hydrodynamics of systems of Brownian particles. *Adv. Phys.* **32**, 173–283 (1983).
69. F. Dallari *et al*., Microsecond hydrodynamic interactions in dense colloidal dispersions probed at the European XFEL. *IUCrJ* **8**, 775–783 (2021).
70. J. D. Maier, J. Wagner, Structure and short-time diffusion of concentrated suspensions consisting of Silicone-Stabilised PMMA particles: A quantitative analysis taking polydispersity effects into account. *Soft Matter* **20**, 1309–1319 (2024).
71. G. C. Abade, B. Cichocki, M. L. Ekiel-Jeżewska, G. Nägele, E. Wajnryb, Short-time dynamics of permeable particles in concentrated suspensions. *J. Chem. Phys.* **132**, 014503 (2010).
72. C. Beenakker, P. Mazur, Diffusion of spheres in a concentrated suspension: Resummation of many-body hydrodynamic interactions. *Phys. Lett. A* **98**, 22–24 (1983).
73. C. Beenakker, P. Mazur, Diffusion of spheres in a concentrated suspension II. *Phys. A Stat. Mech. Appl.* **126**, 349–370 (1984).
74. M. Medina-Noyola, Long-time self-diffusion in concentrated colloidal dispersions. *Phys. Rev. Lett.* **60**, 2705 (1988).
75. A. Van Blaaderen, J. Peetermans, G. Maret, J. Dhont, Long-time self-diffusion of spherical colloidal particles measured with fluorescence recovery after photobleaching. *J. Chem. Phys.* **96**, 4591–4603 (1992).
76. M. Tokuyama, Universality in multicomponent glass-forming liquids near the glass transition. *Phys. Rev. E* **80**, 031503 (2009).
77. H. Löwen, T. Palberg, R. Simon, Dynamical criterion for freezing of colloidal liquids. *Phys. Rev. Lett.* **70**, 1557 (1993).
78. E. R. Weeks, D. Weitz, Properties of cage rearrangements observed near the colloidal glass transition. *Phys. Rev. Lett.* **89**, 095704 (2002).
79. U. Genz, R. Klein, Collective diffusion of charged spheres in the presence of hydrodynamic interaction. *Phys. A Stat. Mech. Appl.* **171**, 26–42 (1991).
80. R. Biehl, Jscatter, a program for evaluation and analysis of experimental data. *PLoS One* **14**, e0218789 (2019).
81. A. J. Banchio, M. Heinen, P. Holmqvist, G. Nägele, Short-and long-time diffusion and dynamic scaling in suspensions of charged colloidal particles. *J. Chem. Phys.* **148**, 134902 (2018).
82. V. Martinez, J. Thijssen, F. Zontone, W. Van Megen, G. Bryant, Dynamics of hard sphere suspensions using dynamic light scattering and x-ray photon correlation spectroscopy: Dynamics and scaling of the intermediate scattering function. *J. Chem. Phys.* **134**, 054505 (2011).
83. P. Segre, P. Pusey, Scaling of the dynamic scattering function of concentrated colloidal suspensions. *Phys. Rev. Lett.* **77**, 771 (1996).
84. M. Tokuyama, Slow dynamics of equilibrium density fluctuations in a supercooled colloidal liquid. *Phys. A Stat. Mech. Appl.* **289**, 57–85 (2001).
85. M. Tokuyama, H. Yamazaki, Y. Terada, Test of mean-field equations for two types of hard-sphere systems by a Brownian-dynamics simulation and a molecular-dynamics simulation. *Phys. Rev. E* **67**, 062403 (2003).

86. A. Leonau *et al.*, A pipeline for megahertz x-ray photon correlation spectroscopy on soft matter samples at the mid instrument of European XFEL. arXiv [Preprint] (2025). http://arxiv.org/abs/2506.08668 (Accessed 10 June 2025).
87. A. M. Raza *et al.*, LTP - MHz XPCS enabled studies of dynamics, interactions and aggregation phenomena in protein solutions (derived from 3348) [Dataset]. European X-ray Free Electron Laser facility. https://doi.org/10.22003/XFEL.EU-DATA-005397-00. Deposited 27 October 2023.
88. A. Lentz *et al.*, LTP - MHz XPCS enabled studies of dynamics, interactions and aggregation phenomena in protein solutions (derived from 3348) [Dataset]. European X-ray Free Electron Laser facility. https://doi.org/10.22003/XFEL.EU-DATA-006996-00. Deposited 8 May 2024.
89. N. D. Anthuparambil *et al.*, Towards microsecond XPCS at the ESRF [Dataset]. European Synchrotron Radiation Facility. https://doi.org/10.15151/ESRF-ES-2009918726. Deposited 27 February 2025.